WILEY

Material design of elastic structures using Voronoi cells

J. M. Podestá[1] | C. G. Méndez[2] | S. Toro[1] | A. E. Huespe[1,3,4] | J. Oliver[3,4]

[1]CIMEC-UNL-CONICET, Predio CONICET Dr Alberto Cassano, Santa Fe, Argentina

[2]CIMNE-Latinoamérica, Santa Fe, Argentina

[3]Centre Internacional de Metodes Numerics a l'Enginyeria (CIMNE), Campus Nord UPC, Barcelona, Spain

[4]Escola Tècnica Superior d'Enginyers de Camins, Canals i Ports, Technical University of Catalonia (BarcelonaTech), Campus Nord UPC, Mòdul C-1, Barcelona, Spain

Correspondence
A. E. Huespe, CIMEC-UNL-CONICET, Predio CONICET Dr Alberto Cassano, CP 3000 Santa Fe, Argentina; or Centre Internacional de Metodes Numerics a l'Enginyeria (CIMNE), Campus Nord UPC, 08034 Barcelona, Spain.
Email: ahuespe@intec.unl.edu.ar

Summary

New tools for the design of metamaterials with periodic microarchitectures are presented. Initially, a two-scale material design approach is adopted. At the structure scale, the material effective properties and their spatial distribution are obtained through a Free Material Optimization technique. At the microstructure scale, the material microarchitecture is designed by appealing to a Topology Optimization Problem (TOP). The TOP is based on the topological derivative and the level set function. The new proposed tools are used to facilitate the search of the optimal microarchitecture configuration. They consist of the following: (i) a procedure to choose an adequate shape of the unit cell domain where the TOP is formulated and shapes of Voronoi cells associated with Bravais lattices are adopted and (ii) a procedure to choose an initial material distribution within the Voronoi cell being utilized as the initial configuration for the iterative TOP.

KEYWORDS
free material optimization (FMO), inverse material design, microarchitecture topology optimization, topology optimization problem (TOP), two-scale material design

1 | INTRODUCTION

In the early 1990s, after the seminal papers of Bendsøe and coauthors,[1,2] the contribution of Ringertz,[3] and the book of Bendsøe,[4] the Free Material Optimization (FMO) methodology has become a well-established technique in the mechanical structural optimization community. This methodology seeks, in a given spatial domain, the optimal distribution of material and its effective properties using the objective of minimum material resource or minimum compliance.

The most specific aspect of this structural optimization methodology is that the minimum of the objective function is sought by assuming a free parameterization of the material elasticity tensor. Hence, it is sometimes called design by the

Symbols for elasticity tensors: C, generic effective fourth-order symmetric elasticity tensor expressed in Cartesian coordinates; C_N, generic effective elasticity tensor expressed in normal form (see Section 2.2.2 and Appendix B); $\hat{C}$, effective elasticity tensor solution of the FMO problems expressed in Cartesian coordinates (Section 3); $\hat{C}_N$, effective elasticity tensor solution of the FMO problems expressed in normal form (Section 3.3); C^*, effective elasticity tensor being the average of $\hat{C}_N$ in a given body sector (Section 3.3); C^h, homogenized elasticity tensor evaluated with a microcell (using a computational homogenization technique, Section 4) expressed in Cartesian coordinates; C_N^h, tensor C^h expressed in normal form; C_{db}^h, homogenized tensor constituting the database (Section 5.2) expressed in normal form; C_μ, microscale elasticity tensor (Section 4).

free parameterization of material. Such as mentioned in section 3.4 in the book of Bendsøe and Sigmund,[5] the formulated optimization problem is general enough and *" … encompasses the design of structural materials in a broad sense, predicting optimal structural topologies and shapes associated with the optimum distribution of the optimized material."*

In the following years, the mathematical basis and new numerical algorithms for the FMO technique have been developed. In fact, some formulations of FMO can be written as convex optimization problems, which satisfy the criterion for guaranteeing the uniqueness of the solution, as shown by Zowe et al[6] and Kočvara et al.[7] Additionally, Kočvara and coauthors have developed optimized algorithms mainly based on nonlinear semidefinite programming procedures for solving very large FMO problems, see the works of Kočvara et al[7] and Stingl et al.[8] Furthermore, efficient primal-dual interior point methods for large-scale problems have been proposed and studied more recently by Weldeyesus and Stolpe.[9]

Intrinsically associated with the FMO methodology is the inverse problem of the material microarchitecture design. In this case, the goal is to find a heterogeneous composite whose effective properties are similar to those required by the FMO solution. Important contributions to reach this objective have also been proposed in the 1990s, particularly in the works of Sigmund,[10,11] who has solved the inverse material design problem using a topology optimization procedure. In this sense, the density-based SIMP (Solid Isotropic Material with Penalization) method has proved to be a very effective tool for solving this kind of inverse homogenization problem.

An FMO technique, jointly with the inverse homogenization problem, as a global two-scale material design methodology, can be utilized as a weakly coupled procedure between the involved scales. First, an FMO technique is employed to compute the effective material properties at large scale, ie, at the structure length scale identified as the macroscale, followed by a technique for designing the microstructure of the heterogeneous composite. Such two-scale technique and variants were worked out by several authors and particularly utilized by Schury et al.[12] Interestingly, this type of two-scale technique does not only provide an optimal material distribution at the macroscale, but also, the requested computational cost is accessible even for attacking 3D problems.

There is, however, an inherent difficulty associated with this two-scale methodology, which is caused by the one-way coupling between scales. In fact, it is not possible to add well-founded mathematical constraints to the FMO formulation to guarantee the microstructure attainability. Such as mentioned by Allaire in his book,[13] from the mechanical point of view, this issue is similar to answer the question on how to characterize the range of the effective properties obtained from a two-phase composite by varying its microstructure. In this context, the microstructure variation is understood as changing either the void fractions, the distributions of the constituent phases, or their elastic properties. From the mathematical point of view, this issue corresponds to finding the G-closure of the set of effective elastic properties obtained from composites with all possible microstructures, see also the work of Cherkaev.[14] Milton and Cherkaev[15] have studied this problem and have determined that any positive definite tensor may be attained using sequential laminates under the condition that a stiff enough material exists. However, positive definite tensor bounds guaranteeing this property with less stringent conditions to that required by the Cherkaev and Milton analysis do not exist, for example, when the stiffness of the composite phases have an upper finite limit. Therefore, this problem is an open issue at the present time.

More recently, there have been intents of including additional manufacture constraints to the FMO problem such as described in the work of Schury.[16] These constraints not only force a gradual spatial change of the effective material properties, but also, they restrict the set of FMO solutions by avoiding the use of extreme materials at the cost of obtaining suboptimal solutions.

From this perspective, additional contributions could be expected by developing new procedures that help in designing microarchitectures with a wide spectrum of attainable effective elasticity tensors. In this paper, we emphasize this specific issue of the problem.

On the one hand, we adopt an FMO technique at the macroscale to determine the material distribution and its effective elastic properties. On the other hand, we employ a topology optimization technique to solve the inverse microstructure design problem. The technique adopted at the microscale is similar to the procedure explained in the works of Amstutz et al and uses the concepts of topological derivative and level set function.[17,18] These two techniques are now well established in the literature, and therefore, no new contributions on these procedures are revealed in this paper.

Instead, the essential contribution here aims to describe two new tools that aid to explore and design a range of periodic material microarchitectures. The principal ideas supporting these contributions are summarized as follows:

1. The first tool is addressed to define the shape of the unit cell domain where the microstructure material inverse homogenization problem is posed. Our numerical experience shows that adequate cell shapes increase the range of elasticity tensors that can be attained through simple microarchitecture topologies. In this sense, it should be noted that certain

topologies may be hidden when only conventional square or rectangular cells subjected to periodic boundary conditions are taken.

The objective that we pursue here is to use a cell shape matching a unit cell shape of the designed periodic material. Thus, by using the symmetry of the effective material properties, we conjecture that the stiff material of the composite is periodically distributed by following a pattern, which can be assimilated to a Bravais lattice having the same class of symmetry as that of the target elasticity tensor. Then, the adopted cell for the topological design problem is a Voronoi cell of this Bravais lattice.

Although the use of polygonal cells for the material inverse design was analyzed in the past by Diaz and Bénard,[19] to the best of our knowledge, the use of Voronoi cells applied to topological design has not been previously considered in the literature.

2. The second of these tools provides a procedure to choose an adequate stiff phase distribution within the Voronoi cell. This configuration is then utilized as the starting point for the topology optimization algorithm determining the final cell configuration.

A brief description of this paper is as follows. The two-scale approach for the material microarchitecture design is briefly revisited in Section 2. Then, the taxonomy of the elastic materials obtained with the structural optimization technique is explored. This classification is utilized for the posterior development of the relevant topics in this paper.

Section 3 gives an overview of two FMO problems that are sequentially solved. The results in terms of extreme materials are analyzed in the same Section.

In Section 4, the adopted methodology for the microstructure design is first presented. Then, Section 5 describes the new tools aforementioned.

In the last section of this paper, we expose the conclusions. Two appendices are finally added. The first appendix describes the FMO discrete formulation and the algorithm to solve this problem. The second appendix deals with issues related to symmetry properties of elastic materials. Moreover, the algorithm to compute the symmetry class and the normal form of an arbitrary elasticity tensor is briefly exposed there.

2 | OVERVIEW OF THE TWO-SCALE–BASED APPROACH

In this work, the approach taken for the optimal material design of a plane elastic structure involves two length scales. The macroscale length ℓ is of the same order of magnitude as that of the structure size, as shown in Figure 1. The microscale length ℓ_μ is of the same order of magnitude as that of the material microarchitecture characteristic length. We assume that $\ell_\mu \ll \ell$.

The macroscale spatial domain is denoted by Ω. It identifies the region where the structure is analyzed and where the optimal distribution of the graduated homogenized material is sought. The material at this scale is characterized by its effective properties, and its optimal distribution is sought by means of an FMO technique.

The material microarchitecture design is defined as an inverse homogenization problem after the optimal elastic effective properties at the macroscale point are known. This inverse problem is solved with a topology optimization technique. The domain Ω_μ denotes the cell where the material is designed. The goal is to find the material distribution within this cell such that the homogenized elasticity tensor, $\boldsymbol{C}^h$, matches a target effective elasticity tensor provided by the FMO technique.
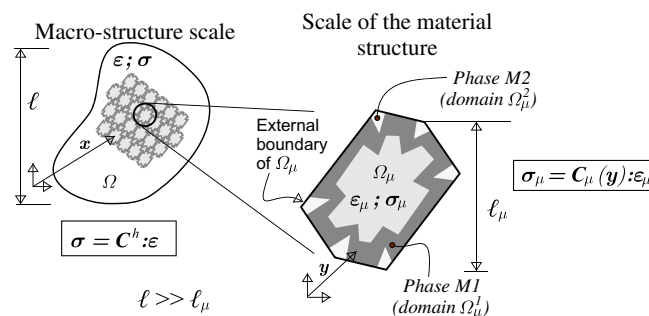

FIGURE 1 Two-scale material design. Notation and entities involved in the analysis. Macroscale domain Ω and microcell Ω_μ [Colour figure can be viewed at wileyonlinelibrary.com]

Vector $\boldsymbol{x}$, as shown in Figure 1, denotes the spatial position of a point at the macroscale. Moreover, vector $\boldsymbol{y}$ identifies the spatial position of a point at the microscale.

Macrostress and macrostrain are denoted by $\boldsymbol{\sigma}$ and $\boldsymbol{\varepsilon}$, respectively. The same entities at the microscale are denoted by $\boldsymbol{\sigma}_\mu$ and $\boldsymbol{\varepsilon}_\mu$. The key material property in this work is the homogenized elasticity tensor $\boldsymbol{C}^h$ at every point $\boldsymbol{x}$ in Ω. This tensor is computed through a conventional homogenization technique. The elasticity tensors of the component phases at the microscale are identified with the symbol $\boldsymbol{C}_\mu$.

It is convenient to remind the standard concepts of unit cell and Representative Volume Element (RVE) utilized for computing effective elastic properties of periodic materials. A unit cell in 2D problems is the smallest area representing the overall behavior of the heterogeneous material, which, with all possible translations along the primitive vectors, fills the full plane without overlapping. Unit cells do not have arbitrary shapes, but they should be adapted in accordance with the periodic material microstructure. Then, conventional periodic boundary conditions are a good choice for computing the homogenized properties utilizing these cells.

Arbitrary cell shapes, not matching unit cell shapes, only represent the overall behavior of the material if they satisfy the condition of being RVEs. This situation occurs, even forcing periodic boundary conditions. In this sense, for a given microstructure, the RVE size should be much larger than the unit cell size; its domain should comprise several unit cells.

An additional important point to be also reminded here refers to Voronoi cells. Periodically structured materials such as crystals with their atomic arrangement represented through Bravais lattices have one particular unit cell, whose geometry preserves the symmetry of the underlying lattice. This unit cell is identified as the Voronoi cell of the Bravais lattice.

2.1 | Sequence of optimization problems

The two-scale material design procedure is performed in three successive stages.

1. Initially, the FMO problem discussed in Section 3 is solved in the spatial region Ω. This domain is chosen with a predefined geometry. The problem solution provides a graded distribution of effective properties given by the effective elasticity tensor $\hat{\boldsymbol{C}} \in \mathbb{S}^+$ in Ω, where $\mathbb{S}^+$ is the symmetric positive definite fourth-order tensor set. Then, considering that $\mathrm{tr}(\hat{\boldsymbol{C}})$ in the FMO formulation represents the pointwise material resource, the subdomains of Ω satisfying the condition

$$\mathrm{tr}(\hat{\boldsymbol{C}}) < \epsilon E_0 \tag{1}$$

   are removed, and the original domain results in a smaller domain Ω^{red}. The parameter ϵ is a small value ($\epsilon \ll 1$), empirically adopted. The parameter E_0 is a reference Young's modulus, typically the modulus of the stiff phase of the designed composite.

   Therefore, after the graded material has been defined in the complete domain through the FMO methodology, the heuristic condition (1) removes the subdomains, where the demanded material resource is low. A similar result can also be obtained using a more formal mathematical technique, for example that based on the topology optimization algorithm described in the work of Giusti et al.[20] Note that the topologies of Ω^{red} and Ω may be different.

2. A second FMO problem is solved in the domain Ω^{red} by imposing the additional constraint

$$(\hat{\boldsymbol{C}} - \delta \boldsymbol{1}) \in \mathbb{S}^+. \tag{2}$$

   The scalar $\delta > 0$ is a small parameter ensuring that all the elasticity tensor eigenvalues are non-null. This constraint has been proposed by Schury[16] as a manufacture restriction.

   Even when constraint (2) generates suboptimal solutions, it facilitates the microstructure design because it fixes lower bounds to the material properties. The effects of this constraint on the material design process are additionally discussed in Section 3.2.

   The solution of the second FMO problem provides the graded distribution of elasticity tensors, $\hat{\boldsymbol{C}}$, in Ω^{red}. Then, a target elasticity tensor, $\boldsymbol{C}^*$, representative of $\hat{\boldsymbol{C}}$ in a given sector of Ω^{red} is defined. The tensor $\boldsymbol{C}^*$ is utilized to design the material microstructure in that sector. Section 3.3 describes the criteria defining these sectors and how $\boldsymbol{C}^*$ is computed.

3. Finally, in a third stage, the microstructure is designed using a topology optimization technique explained in Section 4. The design of the microstructure is performed with $\boldsymbol{C}^*$ as the target tensor.

The new tools for material design proposed in this paper are utilized in the third stage.

2.2 | Characterization of linear elastic materials for optimal structures

Two remarkable features of linear elastic materials arising as the FMO problem solution are their symmetry and stability properties. In this section, we revisit both concepts because they are utilized to predict the shape and orientation of the cell Ω_μ.

2.2.1 | Bimode and unimode unstable materials

Bimode and unimode materials are special subclasses of materials that frequently appear as solutions of optimal structural problems with design criterion related to minimal compliance or minimal material volume. In particular, bimode materials always arise as the optimal FMO solutions of structures subjected to a unique load system, see the work of Bendsøe et al.[1] However, even considering problems with multiple independent load systems,[2] it is possible that optimal solutions would require bimode or unimode materials in some restricted regions of the structure. Both kinds of materials are particularly relevant in this work and analyzed in this Section.

Bimode materials are unstable materials having two easy (compliant) modes of deformation in a 2D space and only one noneasy (hard) mode of deformation. Alternatively, unimode materials have one easy (compliant) mode of deformation and two non-easy (hard) modes of deformation. The elasticity tensors of bimode and unimode materials have two and one null eigenvalues, respectively. Hence, the names bimode or unimode are given to these classes of materials.

Milton and Cherkaev[15] have coined these names in the context of linear elasticity, see also the work of Milton,[21] where additional properties of these materials are analyzed.

Bimode and unimode materials are special classes of linear anisotropic elastic solids. They are characterized by elasticity tensors*

$$C = \sum_{i=1}^{n_m} S_i \otimes S_i, \tag{3}$$

where S_i are symmetric second-order tensors, $n_m = 1$ for bimode and $n_m = 2$ for unimode materials, respectively. For unimode materials, S_1 and S_2 are orthogonal tensors. As usual, the symbol $\otimes$ denotes the tensorial product. In the plane (x_1, x_2), the eigenvector associated with the non-null eigenvalue in bimode materials is $S_1/\|S_1\|$.

Considering (3), for any strain ε, stress σ results in

$$\sigma = C : \varepsilon = (S_1 : \varepsilon)S_1 = -pS_1, \tag{4}$$

where

$$p = -(S_1 : \varepsilon) \tag{5}$$

is a pseudopressure scalar term. In (4), the trace of the tensorial product is denoted by the symbol $(:)$.

In accordance with (4), bimode materials can only support stresses proportional to S_1, with the proportionality factor given by pseudopressures. Therefore, this material collapses when subjected to a different stress state.

2.2.2 | Material symmetry

Symmetry classes of elastic materials are well established in the literature; see, for example, the work of Ting.[22] In Appendix B, we define the four symmetry classes for plane elasticity tensors and summarize the algorithm to compute them. The same algorithm also computes the rotation angle transforming an arbitrary elasticity tensor C, expressed in the Cartesian coordinate system, to its normal form C_N.†

Figure 2 sketches the diagram of set inclusions for the four symmetry classes. Elements of these sets are elasticity tensors. We denote $O(2)$ for isotropic, D_4 for tetragonal, D_2 for orthotropic, and Z_2 for anisotropic symmetries, respectively. From higher to lower symmetry classes, they are: $O(2) \subset D_4 \subset D_2 \subset Z_2$. In the figure, the number of coefficients characterizing a generic elasticity tensor of the corresponding symmetry class is depicted in parenthesis.

Bimode and unimode material sets are also included in the diagram, as well as the relationship between the stability properties of these materials and the symmetry class to which they could belong to. It is remarked that bimode or unimode

---

*Fourth-order tensors are represented by matrices $R^{3\times3}$ using the conventional Kelvin's notation. Consistent with this notation, symmetric second-order tensors are represented by $\varepsilon = [\varepsilon_{11}, \varepsilon_{22}, \sqrt{2}\varepsilon_{12}]^T$ for strains and $\sigma = [\sigma_{11}, \sigma_{22}, \sqrt{2}\sigma_{12}]^T$ for stresses. From now on, we will indistinctly identify a fourth-order tensor by its matrix representation.
†Elasticity tensors in normal axis are denoted with subindex N. The directions of the normal axes for a generic elasticity tensor C are computed with the algorithm of Auffray et al described in Appendix B.
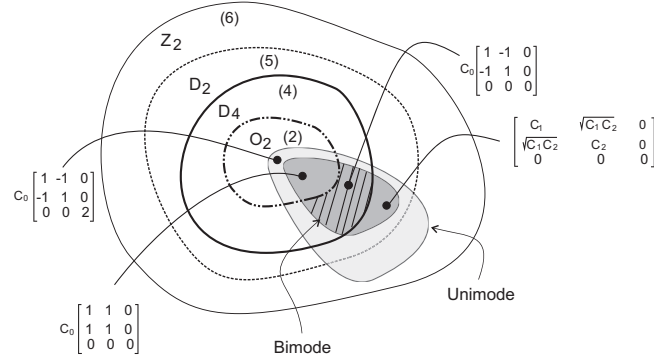
FIGURE 2 Diagram of symmetry class sets for plane elasticity tensors. Symmetry classes are denoted $O(2)$ for isotropic, D_4 for tetragonal, D_2 for orthotropic, and Z_2 for fully anisotropic materials. The number of elastic coefficients defining the elasticity tensors in each class is shown in parentheses. Bimode and unimode material sets are also depicted. C_0, C_1, and C_2 are material parameters

materials with isotropic symmetry, $O(2)$ and bimode materials with tetragonal symmetry, D_4 have elasticity tensors $\boldsymbol{C}_N$ being proportional to those displayed in the Figure 2. They are characterized by only one parameter C_0. Optimal structure solutions demanding bimode materials have been reported by Bendsøe et al[1]; see also the work of Pedersen.[23]

Orthotropic bimode materials have elasticity tensors with the normal form also shown in Figure 2. They are characterized by only two parameters. It is important to remark that a bimode isotropic material has an in-plane Poisson ratio of $\nu = (C_N)_{1122}/(C_N)_{1111} = 1$. On the other hand, a tetragonal bimode material has a ratio of $(C_N)_{1122}/(C_N)_{1111} = -1$.

Important additional observations about this topic are as follows.

1. Bimode materials cannot be fully anisotropic (Z_2).
2. Bimode and unimode materials are characterized with fewer parameters than those required by generic tensors in the corresponding symmetry class.

3 | FREE MATERIAL OPTIMIZATION AT THE MACROSCALE

Free Material Optimization is a useful technique for obtaining the optimal distribution of the material and effective elastic properties in a given spatial domain such that this material configuration satisfies a determined structural requirement. In the present context, the optimization criterion refers to minimum material resource, and the structural requirement refers to the attainment of a limit compliance for a given external force.

3.1 | Problem setting

Let us consider the equilibrium problem of an elastic body in Ω subjected to an external load $\boldsymbol{f}$. The space of displacement fields $\boldsymbol{u}$ in equilibrium with the external forces, $\mathcal{V}^{\text{eq}}$, is

$$\mathcal{V}^{\text{eq}} := \left\{ \boldsymbol{u} \ \middle| \ \int_{\Omega} \nabla^s \boldsymbol{v} : \hat{\boldsymbol{C}} : \nabla^s \boldsymbol{u} \, \mathrm{d}V - \langle \boldsymbol{f}, \boldsymbol{v} \rangle = 0, \quad \forall \boldsymbol{v} \in \mathcal{V} \right\}, \tag{6}$$

where the equilibrium condition is expressed through the conventional virtual work equation, with $\mathcal{V}$ being the space of admissible virtual displacements and $\hat{\boldsymbol{C}}$ being the elasticity tensor.

In the present FMO formulation, the optimization problem consists in minimizing the structural material resource

$$\min_{\hat{\boldsymbol{C}} \in \mathbb{S}^+; \boldsymbol{u} \in \mathcal{V}^{\text{eq}}} \int_{\Omega} \mathrm{tr}(\hat{\boldsymbol{C}}) \, \mathrm{d}V \tag{7a}$$

$$\text{such that} \quad \langle \boldsymbol{f}, \boldsymbol{u} \rangle \leq \bar{f}_u \,, \tag{7b}$$

$$\underline{\rho} \leq \mathrm{tr}(\hat{\boldsymbol{C}}) \leq \bar{\rho} \,, \tag{7c}$$

where the term $\mathrm{tr}(\hat{\boldsymbol{C}})$ represents the pointwise material resource and the design variables are the displacement field $\boldsymbol{u}$ and the elasticity tensor $\hat{\boldsymbol{C}}$. Moreover, $\mathbb{S}^+$ is the space of symmetric positive semidefinite fourth-order tensors, and $\underline{\rho}$ and $\bar{\rho}$ are

the lower and upper bounds imposed to the material resource, respectively. The lower bound $\underline{\rho}$ is a solvability condition imposed to avoid singularities in the structural equilibrium solution. In addition, the upper bound $\bar{\rho}$ is a manufacturability condition that is chosen by considering the higher eigenvalue of the matrix representing the isotropic elasticity tensor of the stiff phase. This eigenvalue is proportional to the Young's modulus, E_0, of the composite stiff phase. Then, we take

$$\bar{\rho} = \beta E_0 , \tag{8}$$

with $\beta < 3$ being an adimensional factor related to the volume fraction of the stiff phase. An empirical rule in material design indicates that the lower the parameter β, the easier it is to find extreme materials with complex mechanism-like microstructures. In (7b), the upper bound for the structural compliance, $\bar{f}_u$, is taken as the compliance computed with the structure constituted by a homogeneously distributed elastic material in Ω, with an elasticity tensor given by $(\beta/3)E_0\mathbf{1}$, where $\mathbf{1}$ is the identity fourth-order tensor.

The optimal solution of problem (7) gives: (i) the spatial distribution of $\hat{\boldsymbol{C}}$; (ii) the symmetry class to which the material belongs to; and (iii) the magnitude of the elastic coefficients.

In structural optimization problems involving several independent load systems, the constraint (7b) is replaced by

$$\sum_{k=1}^{n_{\text{load}}} w_k \langle \boldsymbol{f}_k, \boldsymbol{u}_k \rangle \le \bar{f}_u, \tag{9}$$

where n_{load} is the number of load cases. The k-th load system is defined by the external force $\boldsymbol{f}_k$, and $\boldsymbol{u}_k$ is the associated displacement of the equilibrium solution. w_k (with $w_k \ge 0$ and $\sum_{k=1}^{n_{\text{load}}} w_k = 1$) is a factor weighting each load system. In this case, $\bar{f}_u$ is an upper limit for the weighted average of the compliance.

In Appendix A, we summarize the discretization technique utilized to solve the present FMO formulation and give some details about the algorithm utilized to solve it.

3.2 | Discussion of results obtained with the FMO technique

Discussions of the results obtained with the FMO technique are mainly addressed to analyze the stability, symmetry classes, and additional features of the optimal material properties. This analysis provides basic guidelines for taking adequate decisions in the posterior stage of the microstructure inverse design.

As an empirical rule in the present discussion, we keep in mind that materials demanding high effective shear stiffness jointly with effective in-plane Poisson ratio tending to -1 require the design of complex microstructures.

3.2.1 | First FMO problem

Four conventional structural optimization tests reported in the literature are presented. They are sketched in the first column of Figure 3 and are: (i) L-shaped plate; (ii) cantilever beam; (iii) plate subjected to bending loads, all of them subjected to only 1 load system, f_1. Test (iv) is a plate subjected to three independent load systems, f_1, f_2, and f_3.

The second to fourth columns of Figure 3, as well as Figure 4, display the results of the four tests obtained with the FMO methodology, and $\beta = 0.1$ in Equation (8). These figures show the color maps of the optimal distribution of the following fields.

- **Trace of the normalized elasticity tensors**, $\text{tr}(\hat{\boldsymbol{C}}/E_0)$, ranging from 0.1 to 6×10^{-5}. The material in regions with low values of this field can be removed.
- **Material symmetry classes**. In the tests subjected to only one load system ((i) to (iii)), the optimal materials determined with the FMO problem are bimode materials with symmetries D_4 or D_2. In general, materials with isotropic symmetry $O(2)$ are not observed.
  For the plate subjected to three independent load systems, the optimal solution gives materials with three non-null eigenvalues; compare Figures 3 and 4. In this case, it is also interesting to observe large regions displaying unimode materials with full anisotropy (Z_2) as well as extended regions with bimode materials.
- **Ratio** $(\hat{C}_N)_{1122}/(\hat{C}_N)_{1111}$. The material symmetry classes of optimum solutions computed in tests (i) to (iii) display rather extended regions with tetragonal (D_4) symmetry, meaning that $(\hat{C}_N)_{1111} = (\hat{C}_N)_{2222}$. Therefore, in accordance with the comments remarked in Section 2.2.2, the bimode materials in these regions should necessarily have an in-plane Poisson ratio of value $(\hat{C}_N)_{1122}/(\hat{C}_N)_{1111} = -1$.
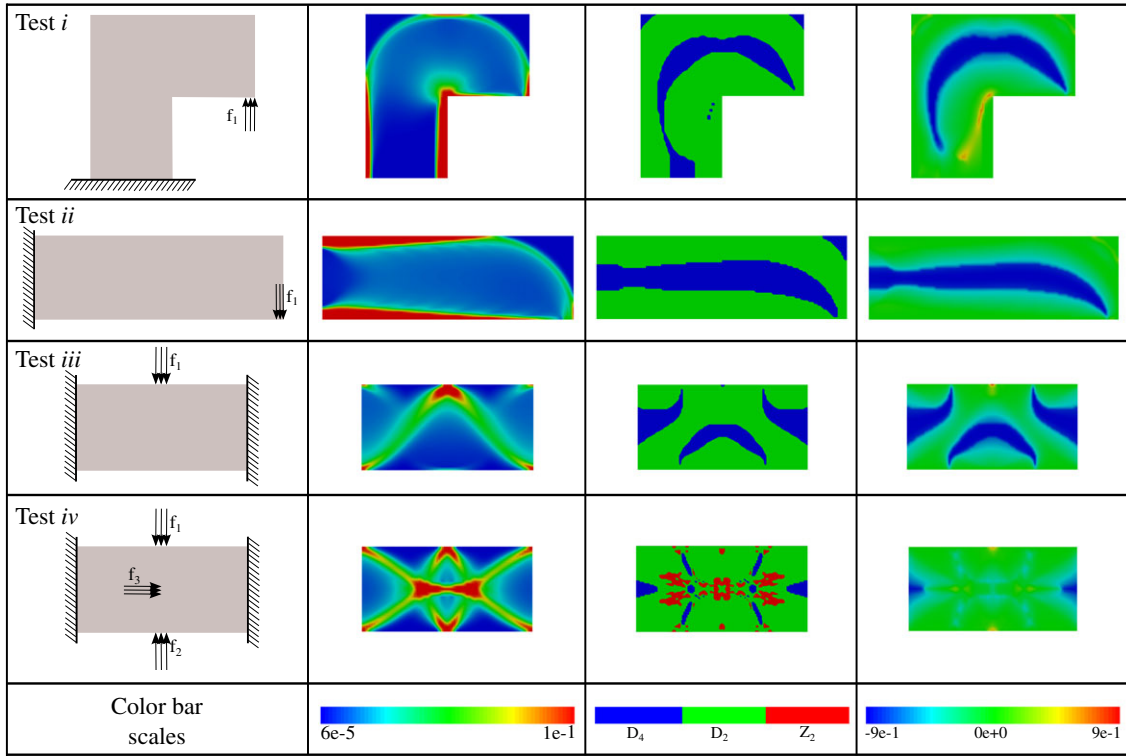
FIGURE 3 Free material optimization results. *First column:* test description; *Second column:* elastic tensor trace; *Third column:* symmetry classes; *Fourth column:* ratio $(\hat{C}_N)_{1122}/(\hat{C}_N)_{1111}$. The condition $(\hat{C}_N)_{1122}/(\hat{C}_N)_{1111} < 0$ defines the regions where the optimal solution requires auxetic materials (zones in blue) [Colour figure can be viewed at wileyonlinelibrary.com]
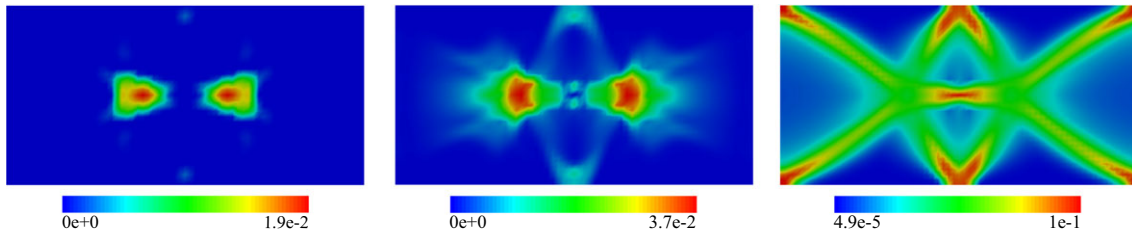

FIGURE 4 Eigenvalues of the elastic tensors for the plate with three independent load systems. Left to right: from smallest to largest eigenvalues [Colour figure can be viewed at wileyonlinelibrary.com]

A further analysis of the ratio $(\hat{C}_N)_{1122}/(\hat{C}_N)_{1111}$ in tests ((i) to (iii)) shows that the optimal solutions in a large part of the structures demand auxetic materials. Roughly speaking, auxetic materials with ratios close to $(\hat{C}_N)_{1122}/(\hat{C}_N)_{1111} \approx -1$ require the design of more complex microstructures with mechanism-like topologies.

- **Smallest non-null eigenvalues of** $\hat{\boldsymbol{C}}/E_0$. Solutions corresponding to only one load system (tests (i) to (iii)) display two eigenvalues equal to zero in the complete structural domain, indicating that a bimodal material is the optimal solution such as reported in the work of Bendsøe et al.[1] Then, the map of the only one non-null eigenvalue is identical to the map of $\mathrm{tr}(\hat{\boldsymbol{C}}/E_0)$. We recall from Equation (3) that bimode material properties have symmetry axes aligned with the principal stress and strain directions.

In Figure 4, we show the distribution of the three eigenvalues of the elasticity tensors obtained as result of the test (iv). Zones with three non-null eigenvalues can be observed. However, there still exist regions with one and two close to zero eigenvalues.

3.2.2 | Second FMO problem

Next, we analyze the results obtained with the second FMO problem with the addition of constraint (2) for the L-plate test. This problem is solved in the reduced domain Ω^{red} that results after adopting a tolerance $\epsilon = 0.015$ in expression (1). The reduced domain Ω^{red} is depicted in Figure 5A.
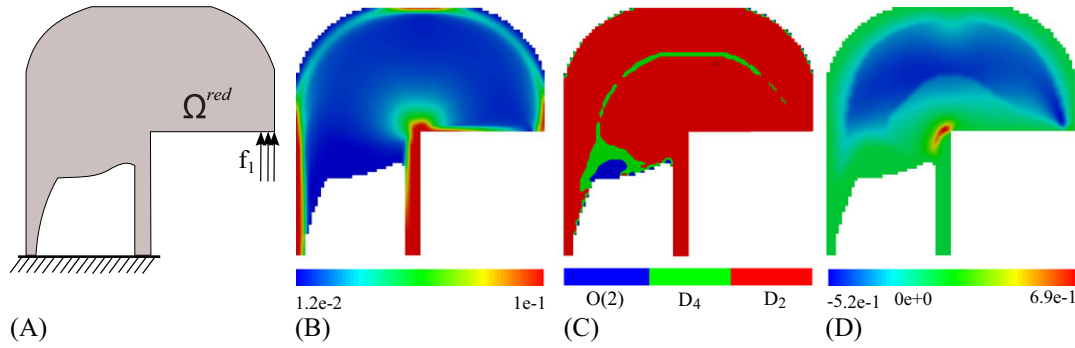
FIGURE 5 L-plate test solved with the second free material optimization problem. A, Reduced domain Ω^{red} after adopting $\delta = E_0/25$; B, Trace of the elasticity tensor ($\text{tr}(\hat{\boldsymbol{C}}/E_0)$); C, Material symmetry classes; D, Ratio $(\hat{C}_N)_{1122}/(\hat{C}_N)_{1111}$ [Colour figure can be viewed at wileyonlinelibrary.com]

We start the analysis by studying first the sensitivity of results with respect to the parameters δ and β introduced in expressions (2) and (8), respectively. Let us consider the role played by parameter δ.

- On the one hand, δ is utilized to suppress solutions yielding extreme materials. This effect is notoriously shown in the FMO solutions for problems with only one load system. In these cases, we have already seen that the resulting elasticity tensors of the first FMO problem corresponds to bimode materials with symmetries D_2 or D_4. Then, the addition of constraint (2) fixes a lower bound for the shear modulus since $(\hat{C}_N)_{1212} \geq \delta/2$. Moreover, it fixes an upper bound for the ratio $|(\hat{C}_N)_{1122}/(\hat{C}_N)_{1111}|$. In fact, being $(\hat{C}_N)_{1111} \geq (\hat{C}_N)_{2222} \geq \delta$, it results to

$$\left|\frac{(\hat{C}_N)_{1122}}{(\hat{C}_N)_{1111}}\right| \leq \sqrt{\left(\frac{(\hat{C}_N)_{2222}}{(\hat{C}_N)_{1111}} - \frac{\delta}{(\hat{C}_N)_{1111}}\right)\left(1 - \frac{\delta}{(\hat{C}_N)_{1111}}\right)} \leq 1. \tag{10}$$

- On the other hand, by comparing with the original FMO problem, the constraint (2) produces suboptimal solutions. The larger the value of δ, the higher the optimal cost function value is.

Both effects are confirmed by analyzing the results shown in Table 1. This table displays the optimal cost functions obtained with different values of δ. In the same table, we also show the corresponding lower and upper values of $(\hat{C}_N)_{1122}/(\hat{C}_N)_{1111}$ in Ω^{red}. We can see that, as δ gets larger, the optimal cost function increases and the extremal values of the field $|(\hat{C}_N)_{1122}/(\hat{C}_N)_{1111}|$ are closer to zero.

In addition, to understand the connection between the parameters β and δ, it should be kept in mind that designing complex materials could be facilitated by taking smaller volume fractions of the stiff phase or, similarly, smaller values of β, see the discussion about this issue in the work of Sigmund.[24] Thus, parameters δ and β have to be adjusted after an adequate trade-off between optimality and manufacturability requirements.

Finally, the parameter ϵ, defining the size of the domain Ω^{red}, is related to δ in the sense that it should be taken as $\epsilon < \delta/E_0$. However, this parameter plays a less important role in the second FMO problem.

3.2.3 | Result obtained with the second FMO problem

Figure 5B displays the field $\text{tr}(\hat{\boldsymbol{C}}/E_0)$ on the domain Ω^{red} of the L-plate problem, only one load system, obtained with $\delta = E_0/25$ and $\beta = 0.1$.

TABLE 1 L-plate test solved with the second FMO problem, $\beta = 0.1$, and different values of parameter δ

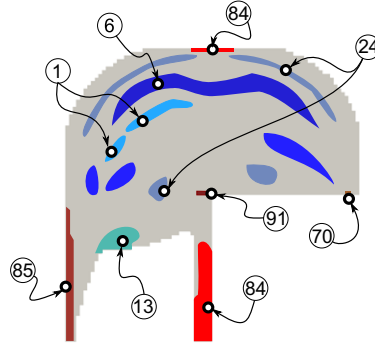| δ/E_0	$\min \int_{\Omega^{\text{red}}} \text{tr}(\hat{C}/E_0) dV$	$\min\left(\frac{(\hat{C}_N)_{1122}}{(\hat{C}_N)_{1111}}\right)$	$\max\left(\frac{(\hat{C}_N)_{1122}}{(\hat{C}_N)_{1111}}\right)$
0	1.89e2	-1.00	1.00
0.020	2.27e2	-0.76	0.95
0.025	2.37e2	-0.71	0.93
0.033	2.52e2	-0.64	0.92
0.040	2.62e2	-0.52	0.65

FIGURE 6 Domain partition criterion for the material microstructure design, $N_{\text{tr}} = N_{\text{poi}} = 13$, $N_{\text{sym}} = 3$, and $n_s = 91$. Only a small number of sectors Ω_i^{red} (with $i = 1, 6, 13, 24, 70, 84, 85, 91$), defined by similar effective elastic properties, are identified in colors [Colour figure can be viewed at wileyonlinelibrary.com]

Figures 5C and 5D show the color maps of the optimum material symmetry classes and their ratio $(\hat{C}_N)_{1122}/(\hat{C}_N)_{1111}$. The distribution as well as the maximum and minimum values are slightly different from those obtained with the original FMO problem on Ω depicted in Figure 3. Notably, in this case, the range of values $(\hat{C}_N)_{1122}/(\hat{C}_N)_{1111}$ are limited to $-0.52 < (\hat{C}_N)_{1122}/(\hat{C}_N)_{1111} < 0.65$, which is a much narrow interval to that displayed by the original FMO solution ranging between $-1 \leq (\hat{C}_N)_{1122}/(\hat{C}_N)_{1111} \leq 1$, see Figure 3. Moreover, in accordance with the constraint (2), the smallest eigenvalue of the elasticity tensor is δ.

3.3 | Domain partition criterion for material design

Once the second FMO problem is solved, the structure domain Ω^{red} is partitioned into disjoint sectors with similar effective material properties. The criterion to define this partition is discussed next.

Given the fields $\text{tr}(\hat{C}/E_0)$ and $(\hat{C}_N)_{1122}/(\hat{C}_N)_{1111}$, we take the following intervals defined by their extreme values:

1. $\mathcal{I}_{\text{tr}} := [\min(\text{tr}(\hat{C}/E_0)); \max(\text{tr}(\hat{C}/E_0))]$
2. $\mathcal{I}_{\text{poi}} := \left[\min\left(\frac{(\hat{C}_N)_{1122}}{(\hat{C}_N)_{1111}}\right); \max\left(\frac{(\hat{C}_N)_{1122}}{(\hat{C}_N)_{1111}}\right)\right]$

and divide them in N_{tr} and N_{poi} proportional subintervals, respectively. In addition, we take the N_{sym} different symmetry classes of the elasticity tensors found in the FMO solution. With these subintervals and classes of symmetries, we can define $N_{\text{tr}} \times N_{\text{poi}} \times N_{\text{sym}}$ sets of elastic properties sharing similar values. Then, it can be defined a natural map relating the $N_{\text{tr}} \times N_{\text{poi}} \times N_{\text{sym}}$ sets of elastic properties to sectors in Ω^{red}, whose points have effective elastic properties lying within the range of the associated sets, with similar elastic properties $\text{tr}(\hat{C}/E_0)$, $(\hat{C}_N)_{1122}/(\hat{C}_N)_{1111}$ and symmetry class. Then, these sectors are denoted Ω_i^{red} with $i = 1, \ldots, n_s$ and n_s is the number of sectors satisfying $n_s \leq N_{\text{tr}} \times N_{\text{poi}} \times N_{\text{sym}}$.

For the L-plate test and taking $N_{\text{tr}} = N_{\text{poi}} = 13$ and $N_{\text{sym}} = 3$, it results in $n_s = 91$ sectors. Some of these sectors are identified in Figure 6.

Finally, for every sector, a representative elasticity tensor $\boldsymbol{C}_i^*$ can be computed as the average

$$\boldsymbol{C}_i^* = \frac{1}{\left|\Omega_i^{\text{red}}\right|} \int_{\Omega_i^{\text{red}}} \hat{\boldsymbol{C}}_N \mathrm{d}V ; \qquad \forall i = 1, \ldots, n_s, \tag{11}$$

where $\left|\Omega_i^{\text{red}}\right|$ is the area of the corresponding ith sector.

The tensor[‡] $\boldsymbol{C}^*$ is taken as the target tensor to design the microstructure using the algorithm described in the following section.

4 | MICROARCHITECTURE DESIGN

Let us consider a two-phase composite constituted by a periodic distribution of a stiff phase M1 and a soft phase M2. Figure 7 represents the microcell of the periodic composite. We seek the distribution of phases M1 and M2 within the

---

[‡]In the following development, subindex i identifying the sector of Ω_i^{red} is dropped out of the notation.
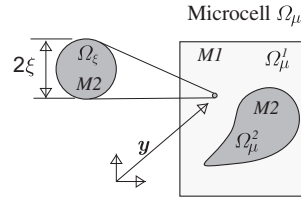
FIGURE 7 Original microcell problem with a material distribution perturbation consisting of introducing a ball Ω_ξ of soft phase within the stiff phase. The radius of the infinitesimal ball is ξ

microcell such that the homogenized elasticity tensor, $C_N^h,^§$ of this composite material is identical to the target elasticity tensor C^* derived from the treatment given to the FMO problem solution in the previous section.

This goal is reached by using an inverse homogenization approach that is formulated as a Topology Optimization Problem (TOP). The TOP is solved in a predefined microdomain Ω_μ with the algorithm proposed by Amstutz and Andrä[17] and Amstutz et al,[18] see also the works of Lopes et al[25] and Méndez et al.[26]

The TOP uses a computational technique for evaluating the homogenized elasticity tensor C_N^h, the topological derivative concept of the homogenized elasticity tensor, and a function describing the distribution of phases in the microcell. The zero-level set of this function represents the interfaces within the cell.

In this work, we only remark some aspects of the TOP, which have been particularly adapted for solving the present inverse homogenization problem. They are the TOP cost function, the imposed constraints, and the augmented Lagrangian technique. Other more conventional aspects of the topology optimization algorithm such as the topological derivative expression are not addressed here because they have been extensively treated in the aforementioned literature.

4.1 | Inverse material design as a TOP

Let us consider a microcell, Ω_μ, of the periodic composite constituted by isotropic elastic phases M1 and M2 occupying the domains Ω_μ^1 and Ω_μ^2, respectively, see Figure 7. The corresponding elastic tensors of both phases are $C_\mu^2 = \gamma C_\mu^1$ with γ being a contrast factor. The characteristic and contrast functions in Ω_μ are defined by

$$\chi(\boldsymbol{y}) = \begin{cases} 0, & \forall \boldsymbol{y} \in \Omega_\mu^2 \\ 1, & \forall \boldsymbol{y} \in \Omega_\mu^1 \end{cases} \quad ; \quad \rho(\boldsymbol{y}) = \begin{cases} \gamma, & \text{if : } \chi = 0 \\ 1, & \text{if : } \chi = 1, \end{cases} \tag{12}$$

respectively. Evidently, the homogenized elasticity tensor C^h of the composite depends on the way in which phases M1 and M2 are distributed in Ω_μ. This dependence is made explicit by introducing the notation $C^h(\chi)$.

Next, we redefine the microarchitecture inverse design problem as a topology optimization problem expressed as follows. Given the target effective elasticity tensor C^*, find the characteristic function χ satisfying

$$\min_\chi \int_{\Omega_\mu} \chi \, \mathrm{d}\Omega$$

$$\text{such that } \left\| C_N^h(\chi) - C^* \right\| = 0 . \tag{13}$$

The cost function represents the stiff phase volume fraction. In particular, considering that the soft phase is void, problem (13) identifies a minimum weight problem.

4.2 | Algorithm for solving the TOP

The TOP (13) can be solved by introducing a level set function $\psi \in C^0(\Omega_\mu)$ defined by

$$\psi(\boldsymbol{y}) = \begin{cases} < 0, & \forall \boldsymbol{y} \in \Omega_\mu^2 \\ > 0, & \forall \boldsymbol{y} \in \Omega_\mu^1 \\ 0, & \text{in the interfaces} \end{cases} \tag{14}$$

§The microstructure design is performed on the normal basis.

jointly with an augmented Lagrangian technique. In this case, the problem is rewritten as follows:

$$\max_{\lambda} \min_{\psi} \mathcal{T}(\psi, \lambda), \tag{15}$$

with

$$\mathcal{T}(\psi, \lambda) = \int_{\Omega_{\mu}} \chi(\psi) \, \mathrm{d}\Omega + \lambda \left(\left\| \boldsymbol{C}_N^h(\psi) - \boldsymbol{C}^* \right\| \right) + \frac{\alpha}{2} \left(\left\| \boldsymbol{C}_N^h(\psi) - \boldsymbol{C}^* \right\| \right)^2, \tag{16}$$

where λ is the constraint Lagrange multiplier and α is a penalty parameter.

The algorithm for solving problem (15) utilizes two nested loops. In an internal loop, the objective function $\mathcal{T}$ is minimized by holding fixed λ and α. This loop, with index denoted k, consists of a level set function–based iteration. While an external loop, with index denoted l, modifies iteratively λ.

The minimum of $\mathcal{T}$ in the internal loop is searched with a descent direction algorithm. For problem (15), the topological derivative is given by

$$D_{\psi} \mathcal{T}(\psi, \lambda) = 1 - \left(\left(\lambda - \alpha \left\| \boldsymbol{C}_N^h - \boldsymbol{C}^* \right\| \right) \frac{(\boldsymbol{C}_N^h - \boldsymbol{C}^*) : D_{\psi} \boldsymbol{C}^h}{\left\| \boldsymbol{C}_N^h - \boldsymbol{C}^* \right\|} \right), \tag{17}$$

where $D_{\psi} \boldsymbol{C}^h$ is the topological derivative of the homogenized elasticity tensor, see the work of Amstutz et al[18] for an additional description of this term. Then, we define the function

$$g(\boldsymbol{y}) = \begin{cases} -(D_{\psi} \mathcal{T}), & \text{if} : \psi < 0 \\ +(D_{\psi} \mathcal{T}), & \text{if} : \psi > 0. \end{cases} \tag{18}$$

The updating formula for ψ, at the $(k + 1)$-th internal loop, is defined by

$$\psi^{k+1} = \psi^k + \tau g, \tag{19}$$

with the scaling factor τ being determined by means of a line search technique.

In the $(l + 1)$-th external loop, the Lagrange multiplier λ is updated using the Uzawa algorithm

$$\lambda^{l+1} = \max \left(0, \lambda^l + \alpha \left\| \boldsymbol{C}_N^h - \boldsymbol{C}^* \right\| \right). \tag{20}$$

The penalty parameter α is held fixed during the full process.

A local optimality criterion of problem (15), see the work of Amstutz,[27] is given by the condition

$$D_{\psi} \mathcal{T} > 0 \quad ; \quad \forall \boldsymbol{y} \in \Omega_{\mu}, \tag{21}$$

which can be implemented by verifying the equality

$$\arccos \left[\frac{\int_{\Omega_{\mu}} g\psi \, \mathrm{d}V}{\|g\|_{L^2} \|\psi\|_{L^2}} \right] = 0. \tag{22}$$

5 | METHODOLOGY FOR SEARCHING THE OPTIMAL MICROSTRUCTURE

Leaving aside the issue related to existence of solutions,[¶] finding one solution of problem (15) may be difficult, especially when extreme materials are designed. The search of a solution with the algorithm described in Section 4.2 is facilitated by following two procedures that are summarized in Sections 5.1 and 5.2.

5.1 | Selection of the microcell shape Ω_{μ}

The shape of the domain Ω_{μ} is an implicit variable utilized in the inverse homogenization problem (13) that should be defined in advance. Considering that problem (13) searches for an optimal periodic microstructure, this variable plays a major role to find an adequate material microarchitecture adjusting the target elasticity.

A good decision is to choose Ω_{μ} coinciding with the shape of a microstructure unit cell. However, in view that the periodic microstructure is unknown at the moment of solving the inverse homogenization problem, we conjecture that

---

[¶]As aforementioned, this issue can be mitigated through the handling of parameter δ in Equation (2).
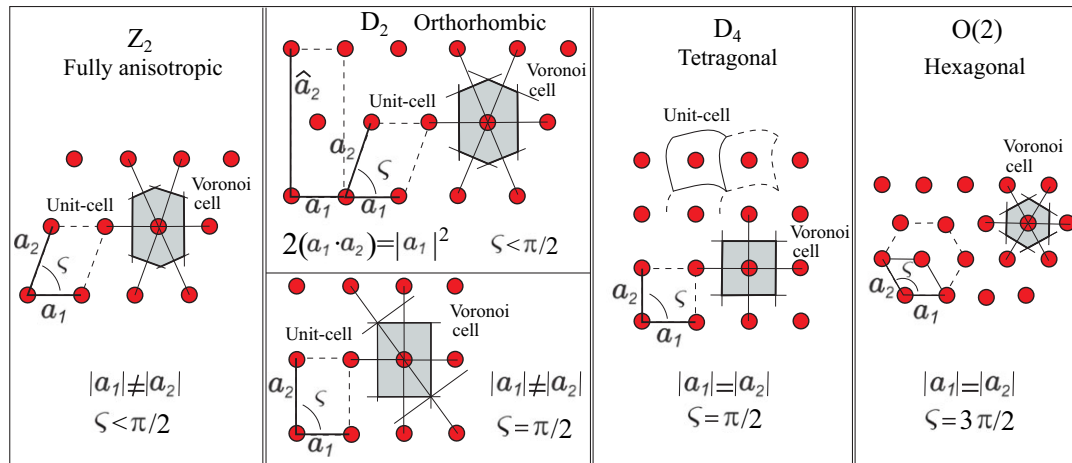
FIGURE 8 Bravais lattices and Voronoi cells (Wigner-Seitz cells) for the material symmetry classes in plane problems. There are only five Bravais lattices in two-dimensions; see the work of Kittel[29] [Colour figure can be viewed at wileyonlinelibrary.com]

the periodic microcell Ω_μ coincides with the shape of the Voronoi cell of a Bravais lattice related to a crystal, which has the elasticity tensor with the same symmetry as that displayed by the target tensor C^*.

In Figure 8, we show the only five different Bravais lattices in 2D and their associated symmetry classes. A Bravais lattice is fully described with the primitive vectors a_1 and a_2. Therefore, Bravais lattices could be described with two parameters, the ratio $\omega = \|a_2\|/\|a_1\|$ and the angle $\varsigma = \arccos[(a_2 \cdot a_1)/(\|a_2\|\|a_1\|)]$. Additional information about this topic can be found in the work of Ashcroft and Mermin.[28]

Moreover, in the same figure, it can be observed that several unit cells are associated with a given Bravais lattice; see, for instance, the unit cells of the lattice with D_4 symmetry.

From all possible unit cells, our interest lies in the Voronoi cells (Weigner-Seitz cells) also depicted in the figure. Voronoi cell shapes preserve the symmetry of the underlying lattice. Observing the lattice with D_4 symmetry, horizontal and vertical directions are axes of symmetry for the lattice; however, they are not symmetry axes for all the unit cells. Instead, the Voronoi cell is symmetric respect to both axes as well as to rotations of ± 90 degrees.

What is more important for the topology optimization problem is that distributing the material within a Voronoi cell with certain spatial symmetry prescribed according to each type of lattice, it can be guaranteed that the symmetry of the underlying lattice is preserved for the homogenized elasticity tensor. Thus, following this criterion, we force the material distribution defined by the level set function in the iterative algorithm of Section 4.2 to satisfy the rotational or reflection symmetries displayed in Figure 9.

Figure 10A displays the plane ω, ς in R^2, where each pair ω, ς defines a Bravais lattice. In gray, we show a bounded space of points with coordinates (ω, ς) defining the full set of all possible Bravais lattices. This reduced space is found by applying symmetry conditions to Bravais lattices. Notice, for example, that the lattice represented in Figure 10B by the point denoted by W′, with coordinates (0.967, 75 degrees), is the same lattice as that represented by the point denoted by W with coordinates (0.5, 30 degrees).
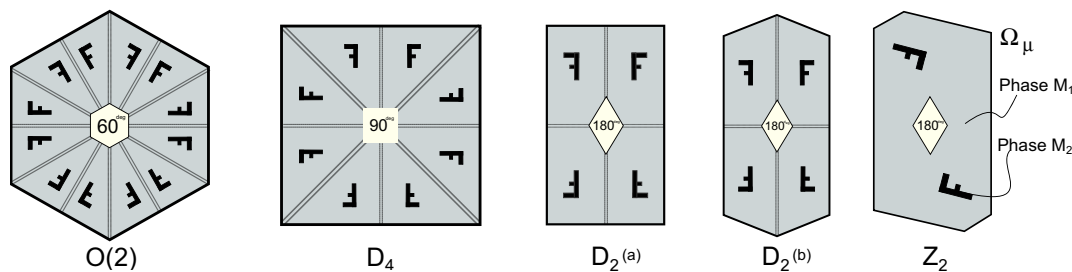

FIGURE 9 Voronoi cell of a 2-phase composite material. Planes and angles of symmetry utilized in the topology optimization algorithm for material distribution. The central symbol indicates the rotation angle preserving the symmetry. Reflection planes are symbolized with double segments [Colour figure can be viewed at wileyonlinelibrary.com]
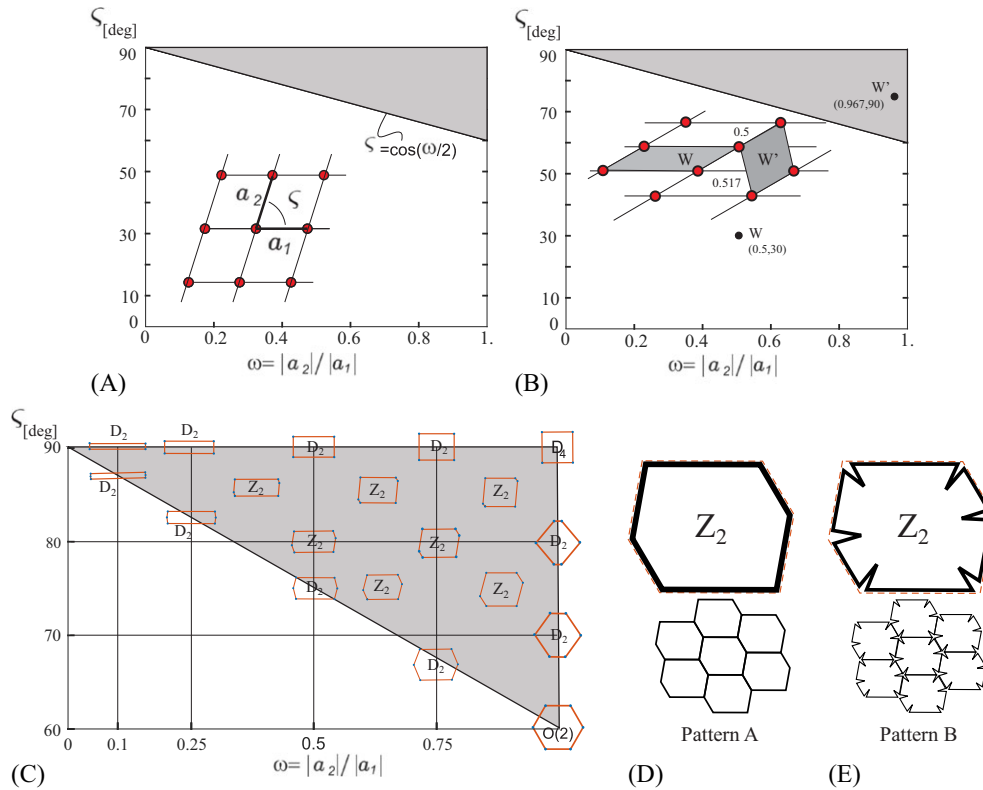
FIGURE 10 Space of parameters ω and ς and microcell shapes. A, Bounded space of parameters ω and ς identifying the complete set of Bravais lattices; B, a Bravais lattice can be represented by two different points, W' and W, in the space ω, ς; C, Voronoi cells and symmetry classes; D and E, Material distribution of Patterns A and B for determining the map $\boldsymbol{C}_{db}^{h}(\omega, \varsigma, f, P)$ [Colour figure can be viewed at wileyonlinelibrary.com]

Figure 10C shows, in the same bounded space, the Voronoi cells associated with different points and the corresponding symmetry classes of these lattices. Thus, in the case that the target elasticity tensor $\boldsymbol{C}^{*}$ has symmetry D_2 or D_4, as it generally happens in FMO problem solutions with only one load system, it should be sufficient to restrict the search of the Ω_μ shape to some of the Voronoi cells represented by the set of parameter ω, ς lying along the boundary of the gray region.

An additional criterion to determine which point (ω, ς) of this set is the most convenient one for choosing the Voronoi cell used in the TOP is described in the following section.

5.2 | Additional criteria to choose the microcell shape and the initial material configuration in Ω_μ

The criteria for choosing a particular Voronoi cell of the space (ω, ς) as well as an adequate distribution of material within this cell, which can be taken as the initial configuration for the iterative algorithm solving the problem (13), are summarily explained here. A full description of this procedure is given in the work of Méndez et al.[30]

Initially, an off-line computation of several homogenized elasticity tensors is performed. These results are used to build a database of homogenized elastic tensors.

The homogenized elastic tensors stored in the data base are the results of several microcell computations with varying shapes and material configurations such as described in the following items:

- Voronoi cells with lattice parameters ω and ς sweeping the entire range of values depicted in gray in Figure 10A;
- Two material configurations denoted Patterns A and B in Figures 10D and 10E. The material configuration of Pattern A corresponds to equal thickness bars of solid material placed on the boundaries of the cells. The Pattern B also corresponds to equal thickness bars placed on the boundaries of the cells but with a re-entrant configuration.
- Several volume fractions f of solid material. This parameter f determines the bar thickness in each case.
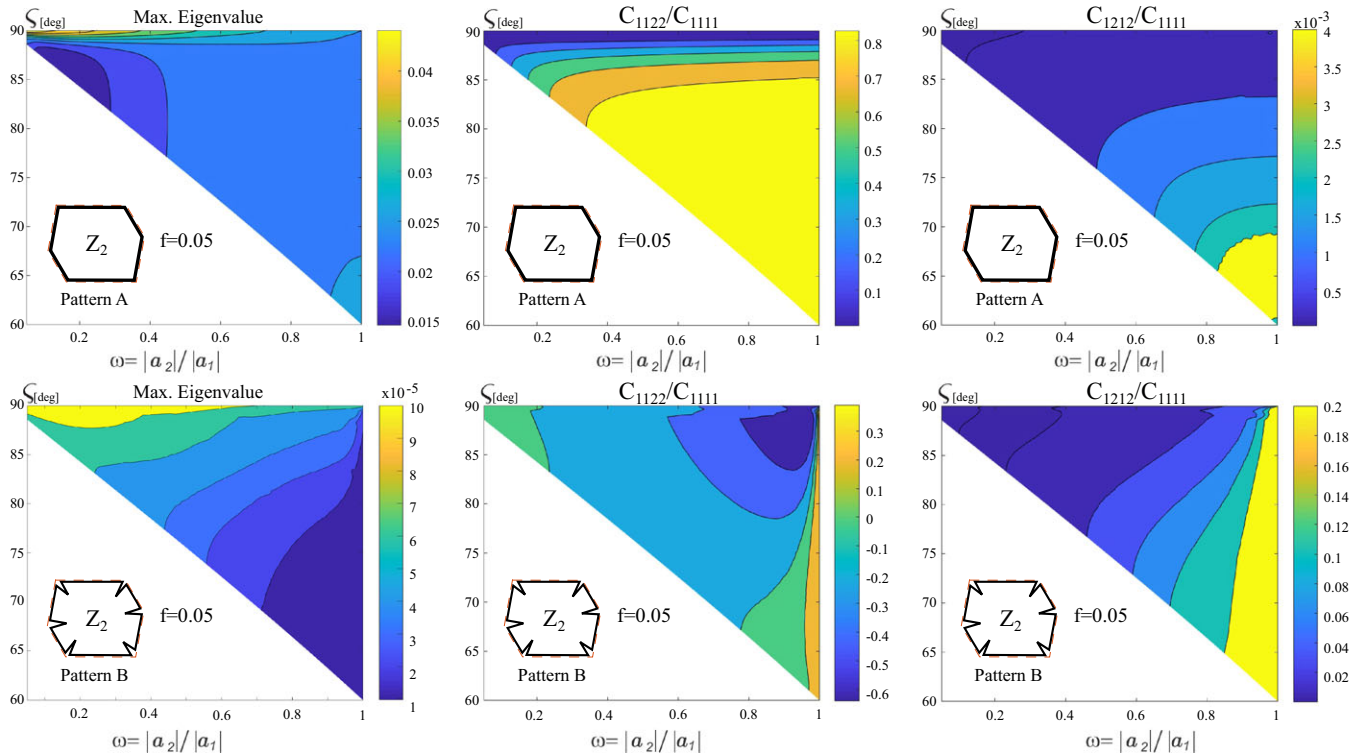
FIGURE 11 Maps of the homogenized elastic properties of Voronoi cells parameterized with ω and ς; the stiff material is distributed according to Patterns A and B and the volume fraction of the stiff phase is $f = 0.05$ [Colour figure can be viewed at wileyonlinelibrary.com]

Therefore, all computed homogenized elasticity tensors in the database can be characterized by four parameters: ω and ς, defining the Voronoi cell shape, and the solid volume fraction f and P, defining the Pattern A or B. We identify each database entry with the notation $\boldsymbol{C}_{db}^h(\omega, \varsigma, f, P)$.

We recall that auxetic materials can be built with re-entrant configurations of bars, see the work of Kolken and Zadpoor.[31] A profuse literature about honeycomb re-entrant auxetic materials exists; see, for example, the work of Fu et al[32] and the references cited therein. The fact of capturing materials with negative ratios $(C_{db}^h)_{1122}/(C_{db}^h)_{1111}$ is the reason why we include Pattern B in the database.

The database is built with a bar material having a normalized Young's modulus[#] $E = 1$ and Poisson ratio $\nu = 0.3$. Several values of f are used. We take approximately $6e3$ points to sweep the reduced domain in the plane (ω, ς). Therefore, the database stores more than $1e5$ homogenized elasticity tensors.

Partial results of this database corresponding to the Patterns A and B and $f = 0.05$ are depicted in Figure 11. These colored maps show in column: (i) the maximum eigenvalue of the homogenized elasticity tensors; (ii) the ratios $(C_{db}^h)_{1122}/(C_{db}^h)_{1111}$; and (iii) the normalized shear stiffness $(C_{db}^h)_{1212}/(C_{db}^h)_{1111}$. As expected, the ratio $(C_{db}^h)_{1122}/(C_{db}^h)_{1111}$ of Pattern B shows a large region of parameters ω, ς defining auxetic microarchitectures. The maximum eigenvalue gives an idea of the maximum stiffness displayed by the respective configuration. Moreover, note the connection between the ratio $(C_{db}^h)_{1122}/(C_{db}^h)_{1111}$ and the shear stiffness for different configurations.

With this database, the most adequate microcell shape and material distribution are adopted by using the criterion

$$\zeta = \arg\left\{ \min_{\boldsymbol{C}_{db}^h} \left\| \boldsymbol{C}_{db}^h(\zeta) - \boldsymbol{C}^* \right\| \right\}, \qquad \text{where } \zeta := \{\omega, \varsigma, f, P\}, \tag{23}$$

which defines the instance of the database that is closer to the target elasticity tensor. The search of the minimum in (23) is restricted to the set of parameters (ω, ς) whose lattices have the same symmetry as $\boldsymbol{C}^*$.

[#] For all configurations displayed in this study, where the soft phase is void, the homogenized elasticity tensor is proportional to Young's modulus of the stiff phase.

5.3 | Results

5.3.1 | L-panel with one load system

Figure 12 shows the microstructures computed with the explained design methodology. The results correspond to nine sectors of the L-panel denoted by 1, 13, 24, 70, 72, 80, 84, 85, and 91, respectively. The unit cells computed for these sectors are depicted such that the horizontal direction coincides with one of the homogenized tensor normal bases. In the same figure, an assembly of several cells is also shown but rotated to the global Cartesian directions. The angle $-\theta$ transforms the normal basis direction to the global Cartesian one. Therefore, θ transforms $\hat{C}$ into $\hat{C}_N$, recalling that $\hat{C}_N$ is used to compute Equation (11). This angle θ is determined for every point of the L-panel.

Figure 13 compares the microcells gathered from the database and those obtained as solution of the TOP. The microcells depicted in the figure correspond to the sectors 1, 13, 24, 80, and 85. Microcells gathered from the database, using the procedure (23), are adopted as the initial configuration for the iterative topology optimization algorithm. Their homogenized elasticity tensor are denoted by C_{db}^h. Alternatively, the homogenized elasticity tensor computed with the microcells being the solution of the TOP are denoted by C_N^h.

Note that the microarchitecture configurations remain rather simple and almost similar to the initial configurations gathered from the database. In addition, observe that the microarchitectures in all sectors are honeycomb-like structures, but the cell shapes change notably in different sectors.

Even when a given sector of the L-panel has similar elastic properties, in accordance with the criterion adopted to define them, explained in the previous section, sectors have nonuniform distribution of the normal basis directions. Therefore, the designed representative microcell for one sector has to be rotated to the physical directions with the angle $-\theta$ at every point of the structure. We evidence this result in Figure 14. There, we depict the designed microstructure for this sector in the physical directions for an identical sector that has been designed with a unique microcell.
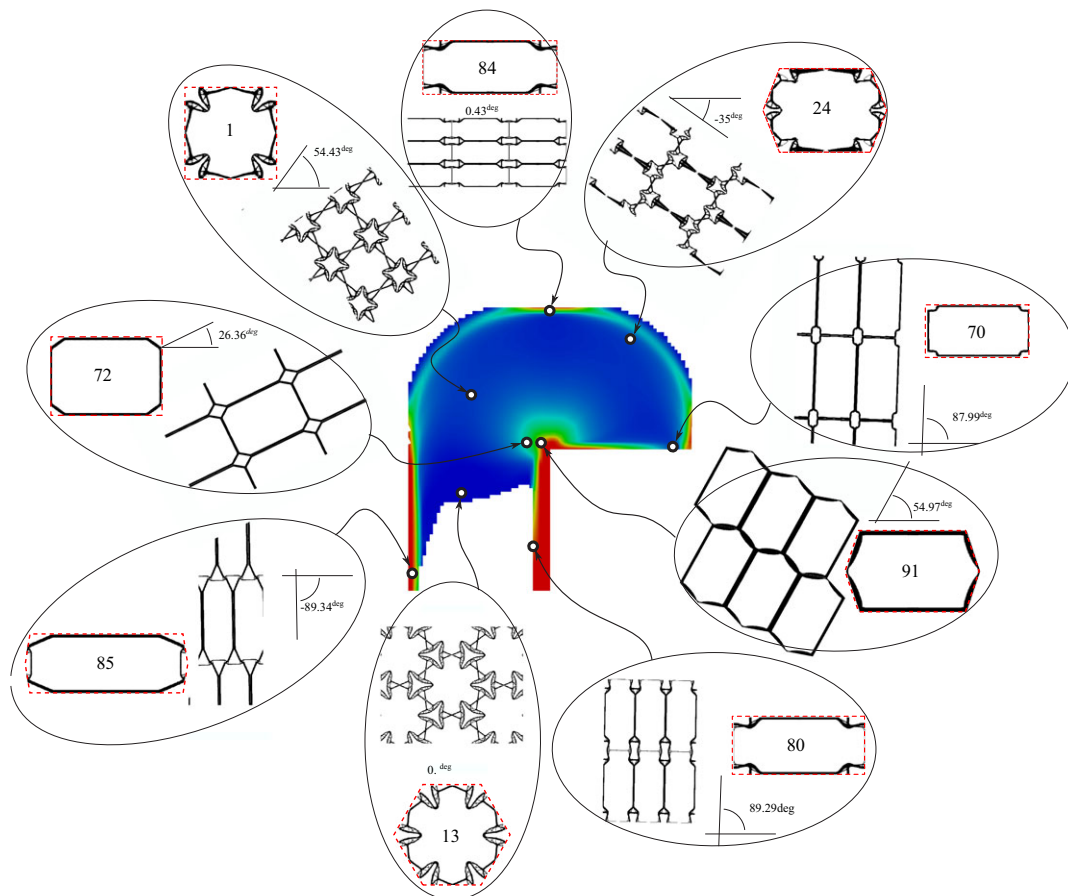

FIGURE 12 Computed microcells for several sectors of the L-panel test. The Cartesian basis of the microcells coincides with the normal basis. Assembled microcells are rotated to the physical directions in each sector [Colour figure can be viewed at wileyonlinelibrary.com]

D_4	1		
$O(2)$	13		
D_2	24		
D_2	80		
D_2	85		

FIGURE 13 L-panel test, microstructure design with the topology optimization problem. The first column reveals the symmetry class of the target elastic tensor. The second column denotes the designed sector. The third column depicts the Voronoi-cell taken from the database as initial configurations for the topology optimization algorithm. The fourth column depicts the Voronoi-cell obtained as solutions of the topology optimization algorithm [Colour figure can be viewed at wileyonlinelibrary.com]
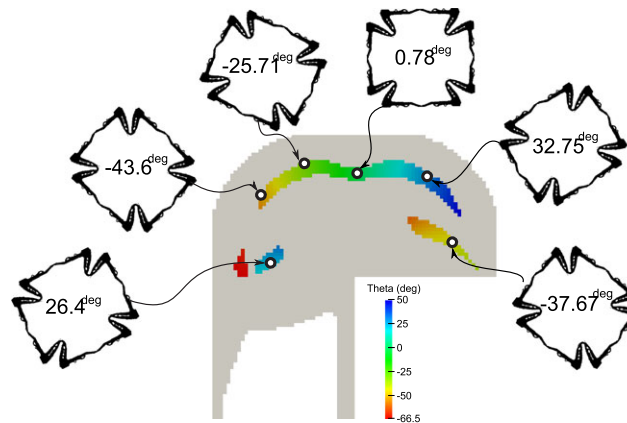

FIGURE 14 Resulting microstructure of Sector 6 rotated to the physical directions. The rotation angle $-\theta$ is shown in accordance with the color scale [Colour figure can be viewed at wileyonlinelibrary.com]

Table 2 displays the components of the target elasticity tensor $\boldsymbol{C}^*$, $\boldsymbol{C}_{db}^h$, and $\boldsymbol{C}_N^h$ in the mentioned sectors, respectively.

Note that, even when the initial configuration value $\boldsymbol{C}_{db}^h$ is close to the target one, the optimization algorithm notably improves the results even without substantially changing the material distribution of the initial configuration. The last column in this table identifies the volume fraction of the gathered and solved microcells.

Note also that from Figure 12 and Table 2, Sector 13 requires a material with isotropic symmetry $O(2)$ as well as an elasticity tensor with zero Poisson ratio and low stiffness. In this case, the re-entrant microstructure designed with the present procedure facilitates the attainment of effective properties with almost zero Poisson ratio.

5.3.2 | Plate subjected to three load systems

Figure 15 shows the microstructures computed for two sectors of the plate subjected to three independent load systems.

The optimal structural result is taken from the first FMO problem solution, see Figure 3, test (iv). In this case, the material with symmetry Z_2 is found in the solution of the FMO problem even without including constraint (2). As the most challenging cases, we design the microstructures of 2 points where the ratio $|C_{1112}^*/C_{1111}^*|$ is maximum. One case corresponds to a tensor with 1 null eigenvalue. The other case corresponds to a tensor with three non-null eigenvalues.

TABLE 2 L-panel test. Topology optimization algorithm results. C^* is the target elasticity tensor, C_{db}^h is the homogenized elastic tensor of the initial configuration (taken from the database), and C_N^h is the homogenized elastic tensor of the converged configuration. Values are multiplied by the factor 1000 ($E_0 = 1$ MPa). The last column displays the volume fraction of the stiff phase

| Sector		C_{1111}	C_{2222}	C_{1212}	C_{2212}	C_{1112}	C_{1122}	Vol. Frac.
1	C_{db}^h	7.93	7.93	0.94	0	0	-1.79	0.30
1	C_N^h	7.19	7.19	1.85	0	0	-3.12	0.17
1	C^*	7.07	7.07	2.00	0	0	-3.07	-
6	C_{db}^h	7.54	4.91	0.65	0	0	-1.61	0.28
6	C_N^h	7.93	5.41	1.14	0	0	-2.28	0.21
6	C^*	7.96	5.37	2.00	0	0	-2.27	-
13	C_{db}^h	4.04	4.04	1.90	0	0	0.24	0.35
13	C_N^h	4.04	4.04	2.01	0	0	0.02	0.14
13	C^*	4.04	4.03	2.00	0	0	0.01	-
24	C_{db}^h	13.73	3.09	1.94	0	0	-0.96	0.40
24	C_N^h	13.22	4.29	1.57	0	0	-1.80	0.15
24	C^*	14.03	4.35	2.00	0	0	-1.85	-
70	C_{db}^h	64.21	6.72	0.09	0	0	13.79	0.12
70	C_N^h	60.99	5.93	0.08	0	0	10.16	0.11
70	C^*	60.75	5.90	2.00	0	0	10.14	-
72	C_{db}^h	48.11	15.27	0.12	0	0	18.55	0.12
72	C_N^h	47.35	13.73	0.07	0	0	20.79	0.10
72	C^*	48.38	14.03	2.00	0	0	21.09	-
80	C_{db}^h	82.81	2.08	2.37	0	0	-2.21	0.40
80	C_N^h	80.15	3.43	0.02	0	0	-0.46	0.12
80	C^*	82.43	4.00	2.00	0	0	-0.37	-
84	C_{db}^h	91.52	1.64	2.20	0	0	-2.29	0.40
84	C_N^h	89.69	3.19	0.02	0	0	-0.18	0.12
84	C^*	91.79	4.00	2.00	0	0	-0.14	-
85	C_{db}^h	93.28	5.66	0.83	0	0	2.04	0.23
85	C_N^h	91.05	3.24	0.22	0	0	1.37	0.13
85	C^*	91.91	4.02	2.00	0	0	0.37	-
91	C_{db}^h	57.25	50.52	0.86	0	0	38.57	0.18
91	C_N^h	60.84	36.03	0.76	0	0	40.68	0.17
91	C^*	60.39	35.61	2.00	0	0	42.16	-
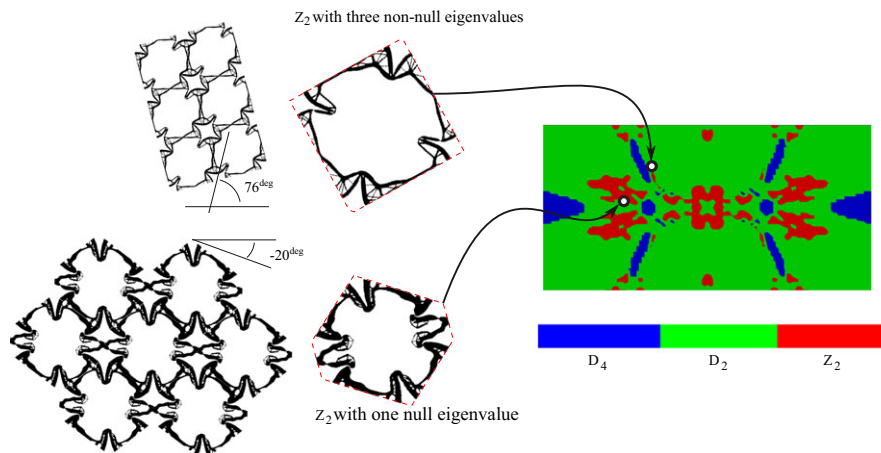
FIGURE 15 Computed microcells for two sectors of the plate subjected to three load systems. The right picture depicts the distribution of symmetry classes. Two microcells are shown. The sectors with these microcells correspond to Z_2 symmetries with 1 null eigenvalue and three non-null eigenvalues, respectively [Colour figure can be viewed at wileyonlinelibrary.com]
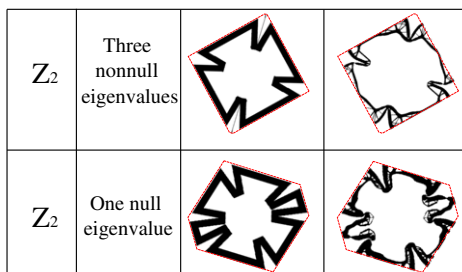
FIGURE 16 Plate subjected to three load systems. Voronoi cell configurations taken for initializing the topology optimization algorithm and the obtained solutions [Colour figure can be viewed at wileyonlinelibrary.com]

TABLE 3 Plate subjected to three load systems. Topology optimization algorithm results for two cases, one of them displays full anisotropic elasticity Z_2. C^* is the target elasticity tensor, C_{db}^h is the homogenized elastic tensor of the initial configuration, gathered from the database, and C_N^h is the homogenized elastic tensor of the topology optimization algorithm converged configuration. Values are multiplied by the factor 1000 ($E_0 = 1$ MPa). The last column displays the volume fraction of the stiff phase

Sector		C_{1111}	C_{2222}	C_{1212}	C_{2212}	C_{1112}	C_{1122}	Vol. Frac.
With 1	C_{db}^h	13.00	5.69	4.68	1.62	-1.62	-0.25	0.45
Null	C_N^h	15.52	3.56	6.72	4.13	-4.60	-2.58	0.29
eigenvalue	C^*	15.63	3.18	6.79	4.63	-4.63	-2.56	-
With 3	C_{db}^h	8.83	8.24	5.35	-2.17	2.17	1.94	0.35
Nonnull	C_N^h	14.41	2.94	6.65	-3.46	3.68	-0.57	0.17
Eigenvalues	C^*	14.38	2.61	6.66	-3.65	3.65	-0.63	-

Figure 16 compares the microcells taken as initial configurations of the topology optimization algorithm with those obtained as solutions of the TOP. Sectors shown in this figure are the same as those depicted in Figure 15.

Table 3 displays the components of the target elasticity tensor C^* in the mentioned sectors. They are also compared with the homogenized elasticity tensors gathered from the database, C_{db}^h, and with the homogenized elasticity tensors computed with the topology optimization algorithm C_N^h.

6 | CONCLUSIONS

In this paper, a two-scale material design approach, coupled in one direction, has been explored. The effective elasticity tensors at the macroscale are computed via a methodology based on a free parameterization of materials. Then, these effective elasticity tensors are used as target tensors for the inverse design of the microarchitectures.

This weakly coupled two-scale approach has been previously reported in the literature. However, the discussions of results obtained with it and presented in Section 3.2 provide the necessary ingredients to state the main contributions of this paper.

These contributions focus on studying two new tools for the inverse design of material microarchitectures in optimal structural problems. They are useful procedures for attaining periodic material configurations with simple honeycomb-like microarchitectures whose effective elasticity tensors cover a wide range. The main characteristics of both tools are summarily described as follows.

1. The first tool defines a rule for the cell shape selection. Then, the TOP is solved in the spatial domain limited by the chosen cell. These cells are the Voronoi cells of Bravais lattices having the same kind of symmetry than the one displayed by the target effective elasticity tensors.
2. The other tool defines an adequate material distribution in the adopted cell. This material distribution is taken as the initial configuration for the iterative topology optimization algorithm.

An additional rule proposed in this paper is the alignment of the Voronoi cell periodicity directions with the natural coordinate system directions of the target elasticity tensor. This rule simplifies the material distribution configurations within the Voronoi cells. In this case, it is necessary to compute the natural coordinate system of every target elasticity tensor.

Both tools, when combined with the aforementioned rule, mitigate the most significant limitation of the two-scale material design methodology described in this paper. This is a remarkable result that is useful for the development of realizable optimal structures using this methodology.

Finally, it is emphasized that the new proposed tools are not only limited to the inverse design of microarchitectures in the context of structural optimization problems, but they also can be applied to other more general types of metamaterial inverse homogenization problems.

ORCID

A. E. Huespe http://orcid.org/0000-0001-7239-9805

REFERENCES

1. Bendsøe MP, Guedes JM, Haber RB, Pedersen P, Taylor JE. An analytical model to predict optimal material properties in the context of optimal structural design. *J Appl Mech*. 1994;61(4):930-937.

2. Bendsøe MP, Díaz AR, Lipton R, Taylor JE. Optimal design of material properties and material distribution for multiple loading conditions. *Int J Numer Methods Eng*. 1995;38(7):1149-1170.

3. Ringertz UT. On finding the optimal distribution of material properties. *Struct Multidiscip Optim*. 1993;5(4):265-267.

4. Bendsøe MP. *Optimization of Structural Topology, Shape, and Material*. New York, NY: Springer-Verlag Berlin Heidelberg New York; 1995.

5. Bendsøe MP, Sigmund O. *Topology optimization approaches: theory, methods, and applications*. Springer-Verlag Berlin Heidelberg; 2003.

6. Zowe J, Kočvara M, Bendsøe MP. Free material optimization via mathematical programming. *Math Program*. 1997;79(1):445-466.

7. Kočvara M, Stingl M, Zowe J. Free material optimization: recent progress. *Optimization*. 2008;57(1):79-100.

8. Stingl M, Kočvara M, Leugering G. A sequential convex semidefinite programming algorithm with an application to multiple-load free material optimization. *SIAM J Optim*. 2009;20(1):130-155.

9. Weldeyesus AG, Stolpe M. A primal-dual interior point method for large-scale free material optimization. *Comput Optim Appl*. 2015;61(2):409-435.

10. Sigmund O. Materials with prescribed constitutive parameters: an inverse homogenization problem. *Int J Solids Struct*. 1994;31(17):2313-2329.

11. Sigmund O. A new class of extremal composites. *J Mech Phys Solids*. 2000;48(2):397-428.

12. Schury F, Stingl M, Wein F. Efficient two-scale optimization of manufacturable graded structures. *SIAM J Sci Comput*. 2012;34(6):B711-B733.

13. Allaire G. *Shape Optimization by the Homogenization Method*. Vol. 146. New York, NY: Springer-Verlag New York; 2012.

14. Cherkaev A. *Variational Methods for Structural Optimization*. Vol. 140. New York, NY: Springer-Verlag Berlin Heidelberg New York; 2012.

15. Milton GW, Cherkaev AV. Which elasticity tensors are realizable? *J Eng Mater Tech*. 1995;117(4):483-493.

16. Schury F. *Two-Scale material design-from theory to practice* [PhD thesis]. Erlangen, Germany: Friedrich-Alexander-Universität Erlangen-Nürnberg; 2013.

17. Amstutz S, Andrä H. A new algorithm for topology optimization using a level-set method. *J Comput Phys*. 2006;216(2):573-588.

18. Amstutz S, Giusti SM, Novotny AA, de Souza Neto EA. Topological derivative for multi-scale linear elasticity models applied to the synthesis of microstructures. *Int J Numer Methods Eng*. 2010;84(6):733-756.

19. Diaz AR, Bénard A. Designing materials with prescribed elastic properties using polygonal cells. *Int J Numer Methods Eng*. 2003;57(3):301-314.

20. Giusti SM, Ferrer A, Oliver J. Topological sensitivity analysis in heterogeneous anisotropic elasticity problem. theoretical and computational aspects. *Comput Meth Appl Mech Eng*. 2016;311:134-150.

21. Milton GW. *The Theory of Composites*. Cambridge, UK: Cambridge University Press; 2002.

22. Ting TC. *Anisotropic Elasticity: Theory and Applications*. Vol. 45. Oxford, NY: Oxford University Press; 1996.

23. Pedersen P. On optimal orientation of orthotropic materials. *Struct Multidiscip Optim*. 1989;1(2):101-106.

24. Sigmund O. *Design of Material Structures Using Topology Optimization* [PhD thesis]. Lyngby, Denmark: Technical University of Denmark; 1994.

25. Lopes CG, dos Santos RB, Novotny AA. Topological derivative-based topology optimization of structures subject to multiple load-cases. *Lat Am J Solids Struct*. 2015;12(5):834-860.

26. Méndez C, Podestá JM, Lloberas-Valls O, Toro S, Huespe AE, Oliver J. Computational material design for acoustic cloaking. *Int J Numer Methods Eng*. 2017;112(10):1353-1380.

27. Amstutz S. Analysis of a level set method for topology optimization. *Optim Methods Softw*. 2011;26(4-5):555-573.

28. Ashcroft NW, Mermin ND. *Solid State Physics*. New York, NY: Harcourt College Publishers; 1976.

29. Kittel C. Introduction to solid state physics. *Univ Pa Law Rev*. 2005;154(3):477.

30. Méndez C, Podestá JM, Toro S, Huespe AE, Oliver J. Symmetry considerations for topology design in the elastic inverse homogenization problem. In preparation; 2017.

31. Kolken HMA, Zadpoor AA. Auxetic mechanical metamaterials. *RSC Adv*. 2017;7(9):5111-5129.

32. Fu MH, Xu OT, Hu LL, Yu TX. Nonlinear shear modulus of re-entrant hexagonal honeycombs under large deformation. *Int J Solids Struct*. 2016;80:284-296.

33. Wächter A, Biegler LT. On the implementation of a primal-dual interior point filter line search algorithm for large-scale nonlinear programming. *Math Program*. 2006;106(1):25-57.

34. Rojas-Labanda S, Stolpe M. Benchmarking optimization solvers for structural topology optimization. *Struct Multidiscip Optim*. 2015;52(3):527-547.

35. Auffray N, Ropars P. Invariant-based reconstruction of bidimensional elasticity tensors. *Int J Solids Struct*. 2016;87:183-193.

36. Cowin SC, Mehrabadi MM. On the identification of material symmetry for anisotropic elastic materials. *Q J Mech Appl Math*. 1987;40(4):451-476.

37. Vianello M. An integrity basis for plane elasticity tensors. *Arch Mech*. 1997;49(1):197-208.

APPENDIX A: DISCRETIZATION OF THE FMO FORMULATION

The finite element method is used to compute the structural response solution and evaluate $\boldsymbol{u} \in \mathcal{V}^{eq}$ as a function of $\hat{\boldsymbol{C}}(\boldsymbol{x})$ and $\boldsymbol{f}$. Conventional bilinear quadrilateral finite elements are used. The elasticity tensor $\hat{\boldsymbol{C}}_i$ is taken to be constant within every i-th finite element, with the indices $i = 1, \ldots, n_{\text{el}}$, and n_{el} is the number of finite elements in the mesh. The symmetry of each tensor $\hat{\boldsymbol{C}}_i$ is enforced by defining only the six independent components, $\hat{C}_{i1111}$, $\hat{C}_{i1122}$, $\hat{C}_{i1112}$, $\hat{C}_{i2222}$, $\hat{C}_{i2212}$, and $\hat{C}_{i1212}$, as design variables for the i-th finite element.

Utilizing this approach, the FMO problem can be rewritten as follows$^{\|}$:

$$\min_{\left(\hat{\boldsymbol{c}}_1, \ldots, \hat{\boldsymbol{c}}_{n_{\text{el}}}, \boldsymbol{u}_1, \ldots, \boldsymbol{u}_{n_{\text{load}}}\right)} \sum_{i=1}^{n_{\text{el}}} \text{tr}(\hat{\boldsymbol{C}}_i)\Omega_i^e \tag{A1a}$$

$$\text{such that } \mathbb{K}\boldsymbol{u}_k - \boldsymbol{f}_k = \boldsymbol{0}; \left(\mathbb{K} = \bigwedge_{j=1}^{n_{\text{el}}} \int_{\Omega_j^e} (\boldsymbol{B}^j)^T \hat{\boldsymbol{C}}_j \boldsymbol{B}^j \, \mathrm{d}V\right); (k = 1, .., n_{\text{load}}) \tag{A1b}$$

$$\sum_{k=1}^{n_{\text{load}}} w_k \langle \boldsymbol{f}_k \cdot \boldsymbol{u}_k \rangle \leq \bar{f}; \tag{A1c}$$

$$\underline{\rho} \leq \text{tr}(\hat{\boldsymbol{C}}_i) \leq \bar{\rho}; \quad (i = 1, \ldots, n_{\text{el}}) \tag{A1d}$$

$$\hat{\boldsymbol{C}}_i \succcurlyeq 0; \quad (i = 1, \ldots, n_{\text{el}}), \tag{A1e}$$

$^{\|}$Introducing an abuse of notation, discrete and continuous fields in this section are identified with the same symbols.

where Ω_i^e is the area of the i-th finite element. Expressions (A1b) are the n_{load} equilibrium equations, one for each independent load system. The stiffness matrix of the discrete equilibrium equations is denoted by $\mathbb{K}$ and is computed with a conventional numerical integration. $\boldsymbol{B}$ denotes the conventional strain-displacement matrix. Expression (A1e) imposes the positive semidefinite character on $\hat{\boldsymbol{C}}_i$.

This FMO problem has $(6 \times n_{\text{el}} + n_{\text{load}} \times n_{\text{dof}})$ design variables, where n_{dof} is the number of degrees of freedom of the finite element mesh (dimension of the interpolated displacement field).

We solve the semidefinite optimization problem (A1) using the IPOPT (Interior Point OPTimizer) primal-dual algorithm, see the work of Wächter and Biegler,[33] with a second-order method. The Hessian matrix is simple to evaluate, but it requires enormous resources of memory. In general, problems presented in this work, up to 10 000 quadrilateral finite elements, need 50 to 70 iterations. Here, we do not pursue the objective of evaluating the computational performance of IPOPT for solving very large-scale problems. For computational benchmarks of structural optimization problems using the IPOPT algorithm, see the work of Rojas-Labanda and Stolpe.[34] Additional information about specific algorithms designed for solving FMO problems can be found in the work of Weldeyesus and Stolpe[9] and references cited therein.

APPENDIX B: SYMMETRIES OF THE ELASTICITY TENSOR IN PLANE PROBLEMS

Let us consider a generic plane elasticity tensor $\boldsymbol{C}$. In the Cartesian coordinate system, its components are denoted by C_{ijkl}, with $i, j, k, l = 1, 2$.

Following the Kelvin's notation, this tensor can be written in the matrix format

$$\boldsymbol{C} = \begin{bmatrix} C_{1111} & C_{1122} & \sqrt{2}C_{1112} \\ C_{2211} & C_{2222} & \sqrt{2}C_{2212} \\ \sqrt{2}C_{1211} & \sqrt{2}C_{1222} & 2C_{1212} \end{bmatrix}. \tag{B1}$$

In addition, $\boldsymbol{C}$ can be expressed in the normal coordinate system (normal basis), see the works of Auffray and Ropars[35] and Cowin and Mehrabadi.[36] The normal coordinate system is rotated an angle θ with respect to the Cartesian coordinate system.

In normal coordinates, the tensor (B1) is represented by the matrix

$$\boldsymbol{C}_N = \begin{bmatrix} K + G + a_1 + d_1 & K - G - d_1 & \sqrt{2}d_2 \\ K - G - d_1 & K + G - a_1 + d_1 & -\sqrt{2}d_2 \\ \sqrt{2}d_2 & -\sqrt{2}d_2 & 2G - 2d_1 \end{bmatrix} \tag{B2}$$

called the normal form of $\boldsymbol{C}$. In this expression, K, G, a_1, d_1, and d_2 are material parameters. The angle θ should also be considered as an additional material parameter. Note that θ is the rotation angle taking the matrix (B1) and transforming it to expression (B2).

According to the symmetry group qualifying $\boldsymbol{C}_N$, these material parameters K, G, a_1, d_1, and d_2 are described as follows.

- Symmetry Z_2 (anisotropic) has six independent elastic coefficients: K, G, a_1, d_1, and d_2 plus the angle θ. The normal form of $\boldsymbol{C}_N$ results with the components $(C_N)_{1112} = -(C_N)_{2212}$.
- Symmetry D_2 (orthotropic) has five independent elastic coefficients: K, G, a_1, and d_1 plus the angle θ. The normal form of $\boldsymbol{C}_N$ results with the components $(C_N)_{1112} = (C_N)_{2212} = 0$ ($d_2 = 0$).
- Symmetry D_4 (tetragonal) has four independent elastic coefficients: K, G, and d_1 plus the angle θ that should be defined such that $a_1 = d_2 = 0$. The normal form of $\boldsymbol{C}_N$ results with the components $(C_N)_{1111} = (C_N)_{2222}$ and $(C_N)_{1112} = (C_N)_{2212} = 0$.
- Symmetry $O(2)$ (isotropic), has two independent elastic coefficients: K and G. The angle θ is arbitrary. Then, the normal form of $\boldsymbol{C}_N$ results with the components $(C_N)_{1111} = (C_N)_{2222}$, $(C_N)_{1212} = (C_N)_{1111} - (C_N)_{1122}$, and $(C_N)_{1112} = (C_N)_{2212} = 0$. In this particular case, we identify

$$\kappa = K - \frac{G}{3}, \tag{B3}$$

where, κ is the 3D bulk modulus and G is the shear modulus.

In all cases, except for isotropic symmetry, the angle θ is an additional parameter of the elasticity tensor.

We recall that the normal format (B2) of $\boldsymbol{C}$ is not preserved in arbitrary Cartesian bases.

B.1 | Reorientation of the elasticity tensor to the normal basis

The rotation angle θ transforming $\boldsymbol{C}$ to the normal axis is found with the algorithm proposed by Auffray and Ropars,[35] see also the work of Vianello.[37]

Auffray et al introduced the fourth- and second-order tensors denoted by $\boldsymbol{D}$, $\boldsymbol{a}$ and the coefficients λ and μ. All these terms are defined as follows:

$$
\begin{aligned}
D_{ijkl} = C_{ijkl} & - \\
& - \frac{1}{6}(\delta_{ij}C_{kplp} + \delta_{kl}C_{ipjp} + \delta_{ik}C_{lpjp} + \delta_{lj}C_{ipkp} + \delta_{il}C_{jpkp} + \delta_{jk}C_{iplp}) \\
& + \frac{C_{pqpq}}{12}(5\delta_{ij}\delta_{kl} - \delta_{ik}\delta_{jl} - \delta_{il}\delta_{jk}) - \frac{C_{ppqq}}{8}(3\delta_{ij}\delta_{kl} - \delta_{ik}\delta_{jl} - \delta_{il}\delta_{jk}) \,, \\
a_{ij} = \frac{1}{12} & (2C_{ipjp} - C_{pqpq}\delta_{ij}) \,, \\
\lambda = \frac{1}{8} & (3C_{ppqq} - 2C_{pqpq}) \,, \\
\mu = \frac{1}{8} & (2C_{pqpq} - C_{ppqq}) \,.
\end{aligned}
\tag{B4}
$$

With these expressions, the invariants of $\boldsymbol{C}$ are calculated

$$
\begin{aligned}
I_1 = \lambda + \mu, \qquad J_1 = \mu, \qquad I_2 = a_{pq}a_{pq}, \\
J_2 = D_{pqrs}D_{pqrs}, \quad I_3 = a_{pq}D_{pqrs}a_{rs}, \quad J_3 = R_{pq}a_{qr}D_{prst}a_{st},
\end{aligned}
\tag{B5}
$$

where the tensor

$$
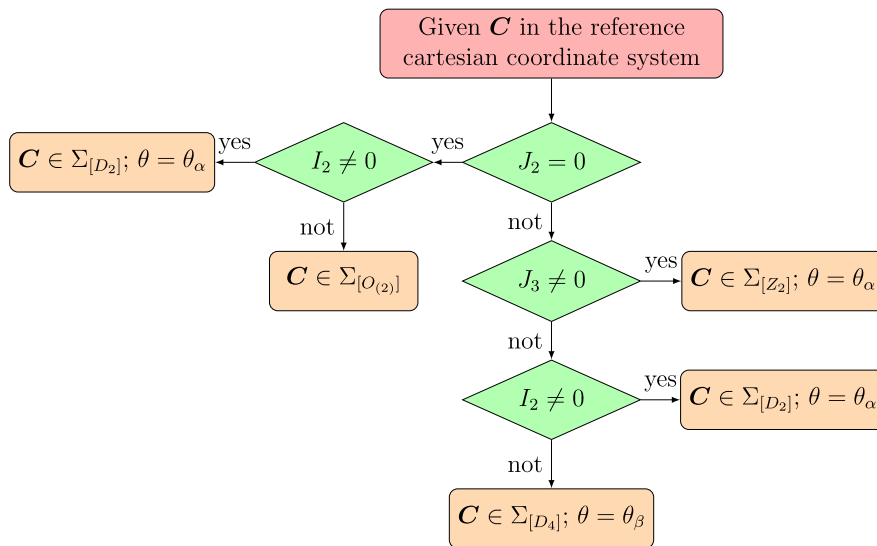R = \begin{pmatrix} 0 & 1 \\ -1 & 0 \end{pmatrix} \,,
$$

FIGURE B1 Classification of $\boldsymbol{C}$-symmetry and angle θ between the normal basis and the Cartesian basis[35] [Colour figure can be viewed at wileyonlinelibrary.com]

These invariants define the symmetry class of $\boldsymbol{C}$. The procedure is described in Figure B1. Moreover, the normal form coefficients of $\boldsymbol{C}$, are determined with expressions (B4) as follows:

$$K = I_1;$$

$$G = J_1;$$

$$a_1 = \frac{1}{2}(a_{11} - a_{22})$$

$$a_2 = \frac{1}{2}(a_{12} + a_{21}),$$

$$d_1 = \frac{\sqrt{8}}{8}(D_{1111} + D_{2222} - D_{1122} - D_{1212} - D_{2112} - D_{2121} - D_{1221} - D_{2211}),$$

$$d_2 = \frac{\sqrt{8}}{8}(D_{1112} + D_{1121} + D_{1211} + D_{2111} - D_{2221} - D_{2212} - D_{2122} - D_{1222}).$$

In addition, defining the angles

$$\theta_\alpha = \frac{1}{2}\tan^{-1}\left(\frac{a_2}{a_1}\right) \quad ; \quad \theta_\beta = \frac{1}{4}\tan^{-1}\left(\frac{d_2}{d_1}\right),$$

the angle θ is determined with the rule $\theta = \theta_\alpha$ for the classes Z_2 or D_2 and $\theta = \theta_\beta$ for the class D_4.